AGU PUBLICATIONS

JGR

Journal of Geophysical Research: Space Physics

RESEARCH ARTICLE
10.1002/2017JA024344

Key Points:
- Terrestrial gamma ray flashes can be accompanied with luminous ionosphere phenomena known as elves
- TGF elves are elve multiplets containing two to four elves, and elve multiplets greater than two are unique ionospheric signatures of TGFs
- Elves associated with intense TGFs can be as bright as the brightest elves caused by cloud-to-ground lightning

Supporting Information:
- Supporting Information S1
- Movie S1
- Movie S2
- Movie S3
- Movie S4
- Movie S5

Correspondence to:
N. Y. Liu,
Ningyu.Liu@unh.edu

Citation:
Liu, N. Y., Dwyer, J. R., & Cummer, S. A. (2017). Elves accompanying terrestrial gamma ray flashes. *Journal of Geophysical Research: Space Physics*, *122*, 10,563–10,576. https://doi.org/10.1002/2017JA024344

Received 9 MAY 2017
Accepted 15 SEP 2017
Accepted article online 19 SEP 2017
Published online 14 OCT 2017

Elves Accompanying Terrestrial Gamma Ray Flashes

Ningyu Liu[1], Joseph R. Dwyer[1], and Steven A. Cummer[2]

[1]Department of Physics and Space Science Center (EOS), University of New Hampshire, Durham, NH, USA, [2]Department of Electrical and Computer Engineering, Duke University, Durham, NC, USA

Abstract This paper reports a modeling study of the optical phenomenon in the lower ionosphere known as elves that may accompany terrestrial gamma ray flashes (TGFs). Recent research has indicated that the in-cloud (IC) discharge processes, termed energetic in-cloud pulses (EIPs), associated with some TGFs can produce a current moment waveform with a peak of hundreds of kA km and a duration of 10 μs. Simulations using the source current moment waveform associated with a Fermi TGF indicate that the radiated electric field at ionospheric altitudes reaches a few times the threshold electric field to excite the optical emissions. A bright elve is therefore induced, with the intensity reaching tens of Megarayleigh, comparable to the brightest elves caused by cloud-to-ground lightning. Because of the strong electromagnetic field radiated, significant blue emissions from the second positive band system of N_2 and the first negative band system of N_2^+ are excited, besides the dominant red emissions from the first positive band system of N_2. The elves caused by EIPs with durations of ~10 μs are elve doublets. For EIPs of longer durations, for example, 30–40 μs, elve multiplets greater than two can be produced. We conclude that elves can be produced by an IC lightning process previously unconnected to elves and that at least some TGFs should have accompanying optical signatures in the lower ionosphere. In addition, TGFs of short durations are more likely to have accompanying elves, because their source currents vary more rapidly.

1. Introduction

Elves are fast expanding rings of optical emissions in the lower ionosphere induced by the electromagnetic field pulses (EMPs) radiated by lightning discharges (e.g., Inan et al., 2010; Liu et al., 2015; Pasko, 2010). They were theoretically predicted by Inan et al. (1991) and have been observed from space (e.g., Boeck et al., 1992; Kuo et al., 2007) and on ground (e.g., Barrington-Leigh et al., 2001; Fukunishi et al., 1996). The modeling study of Inan et al. (1996) found that the EMPs radiated by cloud-to-ground (CG) lightning return strokes with peak currents greater than 80 kA can produce bright ($>10^7$ R) elves at 80–95 km altitudes. A recent analysis of a large number of elve observations has found that the production probability of elves as a function of the peak current fits a linear regression, with a 50% elve probability at 88 kA (Blaes et al., 2016). The elve produced by a CG discharge appears as a thin cylindrical shell of ~30 km thickness, which initially expands at a speed greater than the speed of light and reaches radial distance up to ~250 km (Inan et al., 1996). It forms a ring with the maximum intensity located at radial distance between 40 and 110 km in time-integrated (>1 ms) images, when viewed from a location below the center of the elve. The minimum intensity at the center is due to the minimum in the radiated EMP intensity above the source current. When viewed along an upward slanted direction from the ground, the rapid expansion of the ring results in apparent downward motion. The agreement between the modeling results of Inan et al. (1996) with images and photometric observations of elves has firmly established that elves are driven by lightning EMPs (Barrington-Leigh et al., 2001).

Terrestrial gamma ray flashes (TGFs) are brief bursts (typically <1 ms) of multi-MeV photon radiation originating from thunderclouds in Earth's atmosphere. They were first detected by the Burst and Transient Source Experiment aboard the Compton Gamma Ray Observatory (CGRO) (Fishman et al., 1994) and have since been observed by other spacecraft, including Reuven Ramaty High Energy Solar Spectroscopic Imager (Smith et al., 2005), Astro-rivelatore Gamma a Immagini Leggero (AGILE) (Marisaldi et al., 2010), and Fermi (Briggs et al., 2010). There are currently two competing theories for the physical mechanism generating TGFs in thunderclouds (Dwyer et al., 2012). The first theory is based on the generation of energetic electrons in a region of an extremely large electric field (a few times larger than the conventional breakdown threshold field, E_k) from thermal electrons produced by streamer and leader discharges (Celestin et al., 2012; Moss et al., 2006),

which is known as the cold runaway (also known as thermal runaway or high-field runaway) mechanism. The other theory is relativistic runaway electron avalanches augmented by the relativistic positive feedback mechanism introduced by Dwyer (2003). The resulting discharge, which is capable of generating the required large numbers of energetic electrons in time intervals consistent with the TGF durations, is termed a relativistic feedback discharge (Dwyer, 2012; Liu & Dwyer, 2013).

It has recently been found that at least a subset of TGFs are associated with a special class of in-cloud (IC) discharges, termed energetic in-cloud pulses (EIPs), which are detected by The U.S. National Lightning Detection Network (NLDN) as high peak current (e.g., >150 kA) ICs (Cummer et al., 2014; Lyu et al., 2015). For example, one reported Fermi TGF is produced by an in-cloud discharge event resulting in a current moment of 542 kA km, which would likely have been reported as a >500 kA peak current event if NLDN detectors were not saturated (Cummer et al., 2014). EIPs are, therefore, expected to also produce detectable elves in the lower ionosphere. The study of the elves associated with TGFs is of particular interest to the upcoming TARANIS (Blanc et al., 2007) and ASIM (Neubert et al., 2006) space missions, because their payloads include a suite of instruments dedicated to detecting both energetic particles and optical emissions.

This paper presents a modeling study of the elves caused by EIPs or the elves accompanying TGFs. Because EIPs occur near the top of clouds (Cummer et al., 2014; Lyu et al., 2015), the resulting elves are expected to have similar features as those caused by another class of IC discharges, compact intracloud discharges (CIDs) (Marshall et al., 2015), for example, elves occurring in pairs as "elve doublets" (Marshall et al., 2015; Newsome & Inan, 2010). There are, however, important differences in the properties (e.g., durations and altitudes) of the source currents of EIPs and CIDs, potentially leading to significant differences in the appearance of the elves. Our simulation results indicate that bright elves can be produced by EIPs, and thus TGFs can have accompanying optical signatures in the lower ionosphere. The elves produced by EIPs are typically elve doublets, but under special circumstances, elve multiplets with more than two elves can be induced. As the EMP of an EIP propagates radially outward, the multiplets may merge to form a single elve. For short but bright TGFs, not only the red emissions from the first positive band system of N_2 ($1PN_2$) are produced but also the blue emissions from the second band system of N_2 ($2PN_2$) and the first negative band system of N_2^+ ($1NN_2^+$). It should be noted that in addition to the ionospheric signatures, TGFs can also have accompanying optical emissions near source regions, which may be detectable with high-speed, narrow-band optical instruments (Dwyer et al., 2013; Xu et al., 2015; Xu et al., 2017).

2. Elve Model

The elve model used in our study is similar to what has been used to simulate the elves produced by CGs or CIDs (e.g., Inan et al., 1996; Kuo et al., 2007; Marshall, 2012; Marshall et al., 2015; Veronis et al., 1999). The model simulates the propagation of the EMP pulses, radiated by a discharge current, in the Earth-ionosphere waveguide. At lower ionosphere altitudes, the EMP is reflected due to increasing ionospheric conductivity, while accelerating electrons to energies sufficient to excite air molecules. Azimuthal symmetry is assumed in our model, and cylindrical coordinates are used. The contribution of ions to the ionospheric conductivity is neglected, because the electromagnetic waves of the frequency range relevant to our study are reflected between 80 and 95 km (Inan et al., 2010), where electron density is comparable to the ion density and the conductivity is dominated by electron component because of its much larger mobility (Liu et al., 2015, Figure 2). The electron mobility used to calculate the conductivity depends on electric field, and it decreases rapidly with increasing electric field. In our model, we adopt the electron mobility formula introduced by Salem et al. (2016) to account for the field dependence of electron mobility. According to this formula, the electron mobility is reduced by a factor of ~42 when electric field increases from zero to $0.5E_k$. Note that when the electric field is greater than $0.3E_k$, the excited states leading to $1PN_2$ can be effectively produced (Veronis et al., 1999). The field-dependent mobility introduces nonlinear effects in the simulation, and the reduced mobility (conductivity) at strong electric field allows the lightning EMP to penetrate to higher altitudes in the lower ionosphere. Earth's magnetic field is neglected in the model, because the electron-neutral collisional frequency is larger than the electron gyrofrequency, particularly when the electric field is sufficiently strong to excite optical emissions. Therefore, the ionospheric conductivity tensor (Hu et al., 2007) is reduced to a scalar that depends on the electric field.

Previous studies have found that elves increase electron density in the lower ionosphere by about 20–30% (e.g., Inan et al., 1996). Therefore, the change in the conductivity due to the EMP is dominated by the change in

electron mobility. In addition, electron mobility from various sources often differs more than 10–20% (Salem et al., 2016). We thus ignore the change in the electron density caused by the EMP. The ambient ionospheric density profile used in the model is described by $n_e = n_p = n_0 \exp(-0.15h') \exp[(\beta - 0.15)(h - h')]$ (Wait & Spies, 1964), where $n_0 = 1.43 \times 10^{13}$ m^{-3}, $h' = 84.2$ km, and $\beta = 0.5$ km^{-1} (Hu et al., 2007).

The source current of TGFs is assumed to be uniformly distributed in a cylinder of 500 m radius and 1 km length, centered at 12 km altitude. This size of the source region is consistent with the simulation results of relativistic feedback discharges (Dwyer, 2012; Liu & Dwyer, 2013) and the altitude is consistent with the remote sensing measurements of the EIPs (Cummer et al., 2014; Lyu et al., 2015). A Gaussian distribution in the form of $\exp[-(t-5\sigma)^2/2\sigma^2]$ is assumed for the current waveform, which has been found to be able to generate the radio signals associated with TGFs, particularly short TGFs. We focus on investigating the elves triggered by two current waveforms in the next section. Both have the same peak current moment of 542 kA km (Cummer et al., 2014), but one has a full width at half maximum (FWHM) of 11.2 μs similar to a TGF detected by Fermi on 25 September 2013 (Cummer et al., 2014) and the other has a FWHM of 100 μs, a characteristic timescale of TGFs of longer durations (Briggs et al., 2010; Fishman et al., 2011; Foley et al., 2014). Note that FWHM $= 2.355\sigma$. It should be pointed out that the peak current moment of the longer pulse case is likely unrealistic for EIPs, because the resulting total charge moment change may be too large (Lu et al., 2011).

Simulations were performed with the finite-difference time-domain (FDTD) method, using a freely available software package (Oskooi et al., 2010). Modifications to the code are made to include nonlinear effects related to the field-dependent conductivity. The simulation domain spans 400 km in the radial direction and 100 km in the vertical direction. The ground surface at $z = 0$ km is assumed to be perfectly conducting, and the perfectly matching layer absorbing boundary is used for the boundary at $z = 100$ km or $r = 400$ km. The simulation domain is uniformly discretized with a grid resolution of 125 m, and the time step of the simulation is determined by the FDTD stability condition, with a value of 1.67 μs.

The optical emissions excited by the EMP is simulated by using the model described by Liu and Pasko (2004). Here we focus on investigating the emission intensity of $1PN_2$, which dominates the emissions from elves. The emission intensity in rayleighs is calculated with $I = 10^{-6} A \int_L n\, dl$, where n (cm^{-3}) is the number density of $N_2(B)$ excited particles, A (s^{-1}) is the radiation transition rate, and the integral is taken along the line of sight L (cm). The density n is found by solving a kinetic equation taking into account electron impact excitation, radiation transition, quenching, and cascading (Liu & Pasko, 2004). A coarser grid with a size of 500 m is used to solve the optical emission model, and the electric field needed at the corresponding grid point is found by interpolating the field from the FDTD simulation. The intensity in rayleighs represents an extended emission source with an effective surface emission source. Three representative viewing geometries are considered below. The image of the elve under a particular viewing geometry is shown as if the emitting source is a horizontal surface source at $z = 90$ km or a vertical surface source on the plane containing the z axis. Because elves appear to expand at a speed greater than the speed of light (c), n in the integral for I is evaluated at a source point (x, y, z) on the line of sight at retarded time t_r, that is, $n = n(x, y, z, t_r) = n(r = \sqrt{x^2 + y^2}, z, t_r = t - R/c)$, where R is the distance from the source point (x, y, z) to the observation point.

3. Simulation Results

3.1. The Shorter Pulse Case

The waveforms of the current moment and its time derivative for the shorter pulse case are shown in Figure 1a. Figure 1b shows the corresponding electric field waveform at $r = 100$ km on ground. The solid line gives the simulation results, the dashed and dash-dotted lines are the radiation and induction components of the electric field calculated by using the equation for the electric field radiated by a vertical current (Uman et al., 1975), and the dotted line is the sum of those two components. The radiation component dominates the field at this distance and has the same waveform as the time derivative of the current moment. The simulated field agrees with the analytical solution.

Figure 1c shows the evolution of the radial profile of the normalize electric field E/E_k at $z = 89.5$ km, at which the vertical profile of the normalized electric field at $r = 100$ km has the maximum peak over the entire simulation. The EMP produced by the current pulse propagates away from the source region in the Earth-ionosphere waveguide via multiple reflections between the ionosphere and conducting ground. The field magnitude at each moment of time has four peaks, the leading pair of the peaks corresponds to the two extrema of the time derivative of the current moment waveform, and the lagging pair is the reflection

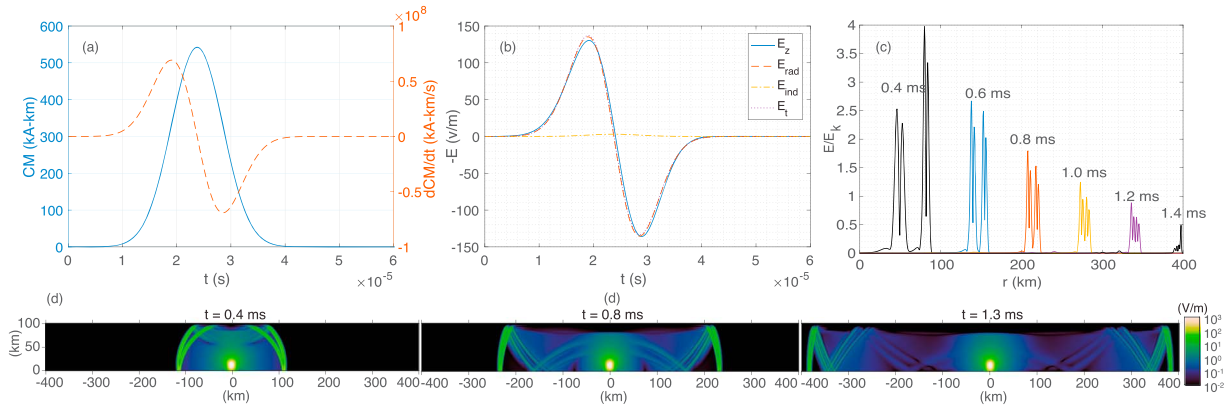

Figure 1. The source current of an EIP of 11.2 μs duration and its electric field. (a) The current moment waveform and its time derivative. (b) The electric field on ground at a distance of 100 km. The solid line shows the field from simulation, the dashed and dash-dotted lines are analytical solutions of the radiation and induction components (Uman et al., 1975), and the dotted line is the sum of those two components. (c) The time evolution of the electric field profile at 89.5 km altitude, at which the vertical profile of the normalized electric field at $r = 100$ km has the maximum peak during the entire simulation. (d) Cross-sectional views of the electric field distribution at 0.4, 0.8, and 1.3 ms.

of the leading pair off the ground. The magnitude of the radiated field decreases with increasing R, the distance from the source to the observation point, as R^{-1} (Uman et al., 1975). As R increases, the time separation between the direct and reflected waves also decreases, because the difference between the direct path and the path via reflection off the ground decreases.

At 0.4 ms, the peaks of the direct wave are well separated from those of the reflected wave. They also have much larger magnitude, because the electric field radiated by a vertical current is proportional to $\sin\theta$ (θ is the angle between $\vec{R}$ and the vertical direction), which rapidly increases with increasing θ when θ is small. The reflected wave can be thought as produced by an image current source located below the ground (Marshall et al., 2015; Uman et al., 1975). The angle θ for the reflected wave at 0.4 ms shown in Figure 1c is much smaller than that for the direct wave, so the magnitude of the reflected wave is smaller. Although not shown here, the magnitude of the reflected wave that reaches the same radial distance as the direct wave at 0.4 ms is still smaller, because θ for the reflected wave is still smaller and the distance from the image source is larger. At later moments of time, θ is much larger because of increased r, and $\sin\theta$ varies only gradually. In this case, the magnitude of the reflected wave is larger, likely because of the strong dependence of the coefficient of the ionosphere reflection on the angle of incidence. At $r > \sim$170 km, the angle of incidence for the ionosphere reflection is greater than 65°, which is larger than the pseudo-Brewster angle shown in Figure 3.48 of (Inan & Inan, 2000), and the magnitude of the reflection coefficient increases with increasing θ. However, the vertical field components of the incident and reflected waves for the ionosphere reflection are out of phase. For the direct wave, a larger ionosphere reflection results from its larger angle of incidence, which cancels a larger fraction of the incident wave field. Thus, the direct wave has a smaller magnitude than the ground-reflected wave. Finally, the peak corresponding to the first extremum of the current moment derivative is smaller than the peak corresponding to the second extremum, likely because of the frequency dispersion of the reflection and transmission coefficients. The frequency dispersion changes the pulse shapes so that the lower frequencies of the first extremum are at the leading peak and its higher frequencies come just a bit later, which diminishes the amplitude of the leading peak relative to the trailing peak.

Figure 2 shows the distributions of the normalized electric field E/E_k and the density of the excited states $N_2(B)$ at 0.4, 0.8, and 1.3 ms. At each moment of time, the distributions of the normalized electric field show that there are four concentric shells of strong electric field, corresponding to the two extrema of the current moment derivative and their reflections. The region in each shell with electric field greater than $0.3E_k$ extends vertically from ~75 to ~95 km altitude. Even as the shells reach the outer boundary of the simulation region, the peak electric fields still exceed $0.3E_k$. Note that E_k is about 20 V/m at 85 km altitude. The number density of the $N_2(B)$ states decreases as the shells reach larger r, consistent with the decreasing magnitude of the electric field. Above ~53 km, the quenching of $N_2(B)$ states can be ignored, and their lifetime is determined by the radiative process. The corresponding Einstein coefficient is 1.7×10^5 s^{-1}, giving a lifetime of about 5.9 μs,

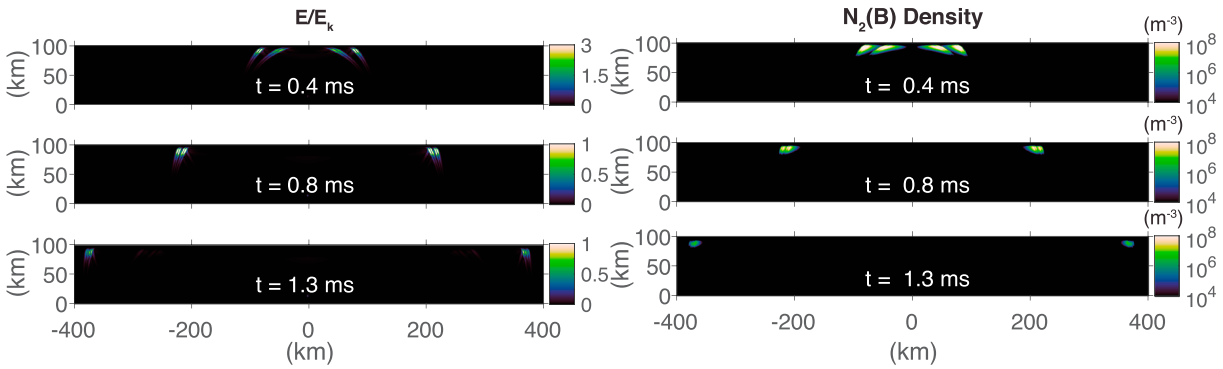

Figure 2. Cross-sectional views of the normalized electric field E/E_k and the density of the excited states $N_2(B)$ giving $1PN_2$ emissions at 0.4, 0.8, and 1.3 ms.

which is slightly larger than half of the FWHM time of the source current waveform. This leads to larger and more diffuse regions of the enhanced number density of the $N_2(B)$ states and less distinct separations between the concentric shells.

The simulated elve viewed under three representative geometries is shown in Figure 3. The fast-expanding elve appears differently in each case. However, the peak instantaneous intensities of the $1PN_2$ emissions all reach tens of millions of rayleighs, and the maxima of the intensities averaged over 1 ms reach about one million rayleighs, although differences in the magnitudes of the averaged intensities of the three viewing geometries are noticeable. When viewed from a spacecraft at 700 km altitude right above the center, the elve has a perfectly circular shape, similar to the view from right below the center (Inan et al., 1996; Marshall, 2012; Veronis et al., 1999). Initially, for example, at 2.54 ms, there are two concentric rings corresponding to the wavefronts of the direct and ground-reflected waves, which indicates that elves associated with TGFs are also "doublets" as those produced by CIDs (Marshall et al., 2015). Note that the substructure in the direct or reflected wave is completely lost in the emission intensity distribution, not only because the lifetime of the $N_2(B)$ states is comparable to the time separation between the two extrema of the current moment derivative, as mentioned earlier, but also because the integration to calculate the emission intensity is taken along a slanted path through an emission region with a vertical thickness of about 20 km. At 3.29 ms, the doublet feature also disappears when the time separation of the electric field peaks from the direct and reflected waves is greatly reduced as shown in Figure 1. The decreasing intensity of the expanding ring, as it moves radially outward, is due to the decreasing magnitude of the EMP. The average intensity shows there is a minimum in the center, consistent with the radiation pattern of a vertical current (Uman et al., 1975) and previous modeling results (e.g., Inan et al., 1996; Marshall, 2012; Veronis et al., 1999) and observations (e.g., Barrington-Leigh et al., 2001) of elves.

If the spacecraft has an additional 700 km horizontal displacement from the center of the elve or the source current, the elve does not appear as a concentric ring anymore, as shown in Figure 3b. The light from the side of the ring closer to the spacecraft arrives earlier. Or the light from the nearside, emitted at a later time when the ring has a larger radius, arrives at the same time as the light from the farside emitted at an earlier time when it has a smaller radius. This results in an apparent oval shape of the elve. Because of the same reason, the electromagnetic field magnitude is smaller at the nearside, and the nearside is not as bright as the farside. In addition, the slanted path for the integration is longer for the farside, also contributing to making the farside brighter. The latter reason explains why the average intensity also shows a brighter farside. It should be noted that the elve is simulated only up to the moment when the EMP reaches 400 km in the radial direction. This is why a section of the ring is missing in the nearside at 3.89 and 4.27 ms. Finally, the left sharp edge of the averaged intensity is formed because the average is calculated over the first 1 ms after the light from the elve first reaches the spacecraft and the light emitted beyond the left edge has not arrived yet.

If the observation is made from a point ($x = 600$ km, $y = 0, z = 0$) on ground, the elve projected on the yz plane is shown in Figure 3c. The expanding ring is first seen when it reaches about 300 km in the radial direction, which gives the shortest path from the current source to the observation point via ionospheric reflection. It is projected to ~180 km altitude on the yz plane. As time progresses, the light emitted earlier from the nearside of the ring arrives. The smaller radius of the ring at earlier moments of time means that it is farther away

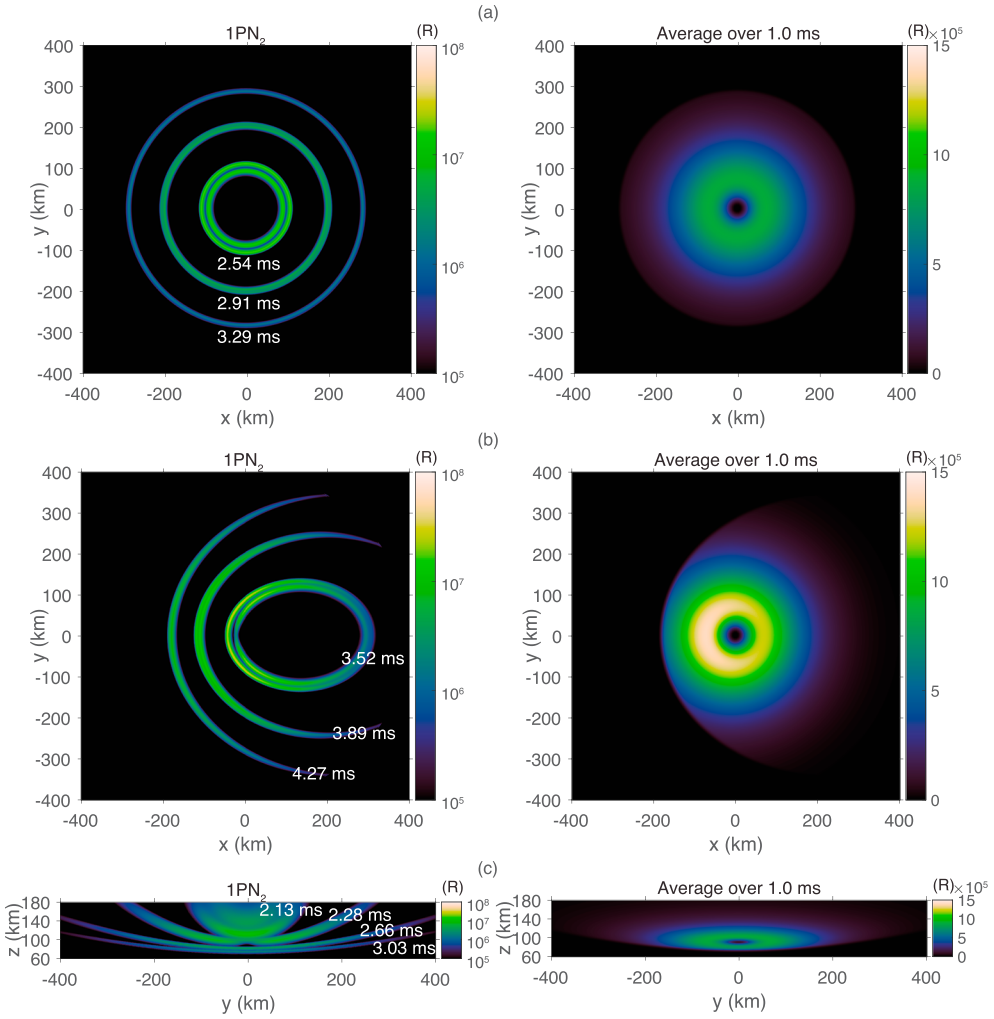

Figure 3. The elve projected at 90 km altitude when viewed from a spacecraft at 700 km altitude (a) right above the center and (b) with a horizontal displacement of 700 km from the center. (c) The elve projected on the *yz* plane, viewed from a point at $x = 600$ km. Taking into account Earth's curvature, the viewing point is at 28 km altitude. The left panels show the instantaneous intensity in rayleighs at selected moments of time, and the right panels show the intensity averaged over 1 ms (also see Movies S1, S2 and S3 included as supporting information).

from the observation point. The corresponding projection on the *yz* plane is lower in the altitude, creating an impression of a descending motion. The light from the side section of the ring arrives later than the nearside, and the projected altitude is higher due to the same reason, forming an arc shape in the *yz* plane. At 2.13 ms, the doublet feature of the elve is discernible, with the emissions corresponding to the reflected wave seen at higher altitudes. The averaged intensity distribution with an oval shape hole at the center is consistent with previous observational and modeling results (Barrington-Leigh et al., 2001; Marshall, 2012).

3.2. The Longer Pulse Case

The waveforms of the current moment and its time derivative for the longer current pulse case with a 100 μs FWHM are shown in Figure 4a. Figure 4b shows the agreement between the simulated electric field with the analytical solution. Compared to the shorter pulse case, the relative contribution from the induction component to the electric field is larger, because the radiation component is smaller due to slower variation of the current moment, while the peak of the induction component is the same because the current moment peak is the same. Figure 4c shows the evolution of the waveform of the normalized electric field at $z = 86.5$ km, at which the profile of the normalized electric field at $r = 100$ km has the maximum peak during the entire simulation. This altitude is 3 km lower than that for the shorter pulse case, which is expected because the EMP from the longer current pulse has more low-frequency content and is reflected by the ionosphere at lower altitudes.

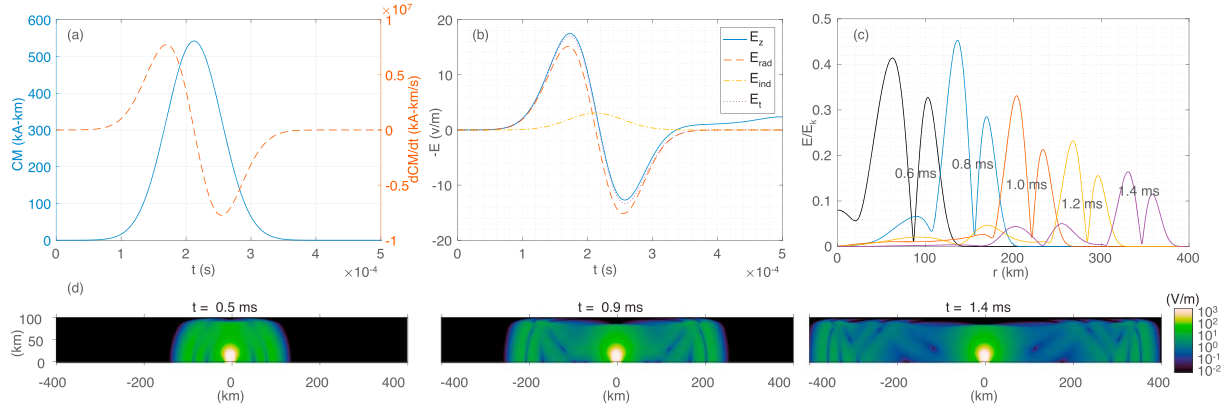

Figure 4. The source current of an EIP of 100 μs duration and its electric field. (a) The current moment waveform and its time derivative. (b) The electric field on ground at a distance of 100 km. The solid line shows the field from simulation, the dashed and dash-dotted lines are analytical solutions of the radiation and induction components (Uman et al., 1975), and the dotted line is the sum of those two components. (c) The time evolution of the electric field profile at 86.5 km altitude, at which the normalized electric field, E/E_k, at $r = 100$ km has its maximum value over the entire simulation. (d) Cross-sectional views of the electric field distribution at 0.5, 0.9, and 1.4 ms.

Also different from the shorter pulse case is that the field profile at each moment of time only has two peaks. The time separation between the two extrema of the current moment derivative is $2\sigma = 85$ μs. The extra distance that the reflected wave off the ground propagates along a vertical path is about 24 km, equivalent to 80 μs, and this time is reduced for a slanted path. As a result, the reflection from the first extremum of the current moment waveform overlaps with the direct wave from the second extremum so that each extremum loses its identity. This also results in a stronger second peak in the figure. At 0.6 ms, the electric field at $r = 0$ is significant compared to its peak, and it can be even larger at earlier moments of time, for example, $> 0.4E_k$ at 0.5 ms. The field at $r = 0$ is due to the induction component. This indicates that the current moment is so large that the induction component is sufficient to excite $1PN_2$ right above the EIP discharge. Shortly after the EMP passes 200 km in the radial direction, its magnitude drops below $0.3E_0$ and the production of $N_2(B)$ states is negligible.

The distributions of the normalized electric field and the density of the excited states $N_2(B)$ in Figure 5 show that the regions with enhanced electric field or $N_2(B)$ density are more diffuse than those for the shorter pulse case, but with much smaller magnitudes. Two concentric shells are visible in the normalized electric field throughout the simulation, corresponding to the direct and ground-reflected waves, respectively. The $N_2(B)$ density distribution has two concentric shells at 0.5 and 0.9 ms, but only one shell at 1.2 ms because of the decreased field magnitude. The trailing shell also has a larger density magnitude. The excitation of $N_2(B)$ states above the center initially is caused by the induction component of the electric field.

The elve viewed from the same three observation points as previously is shown in Figure 6. Both of the instantaneous and average intensities are about 3 orders of magnitude smaller than the previous case. The shape of the elve under each view is similar to the previous case, but the spatial extension is smaller. A noticeable

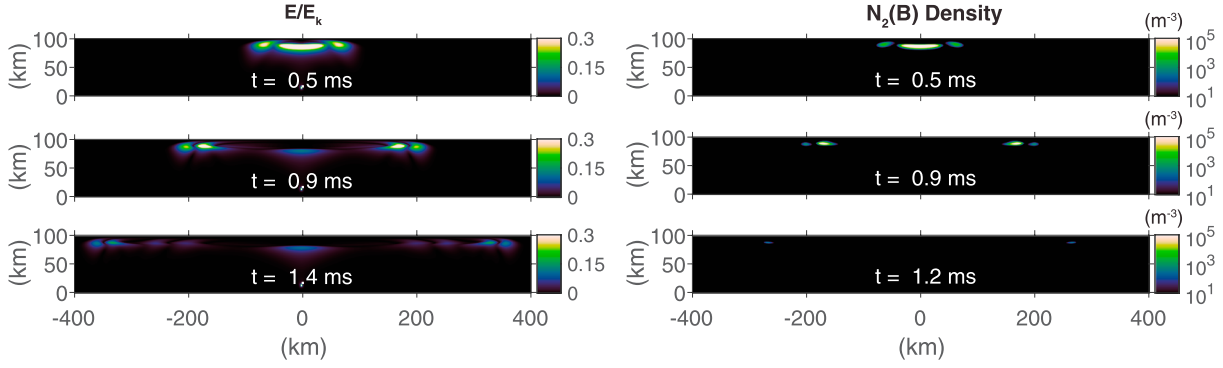

Figure 5. Cross-sectional views of the normalized electric field E/E_k at 0.5, 0.9, and 1.4 ms, and the density of the excited states $N_2(B)$ at 0.5, 0.9, and 1.2 ms.

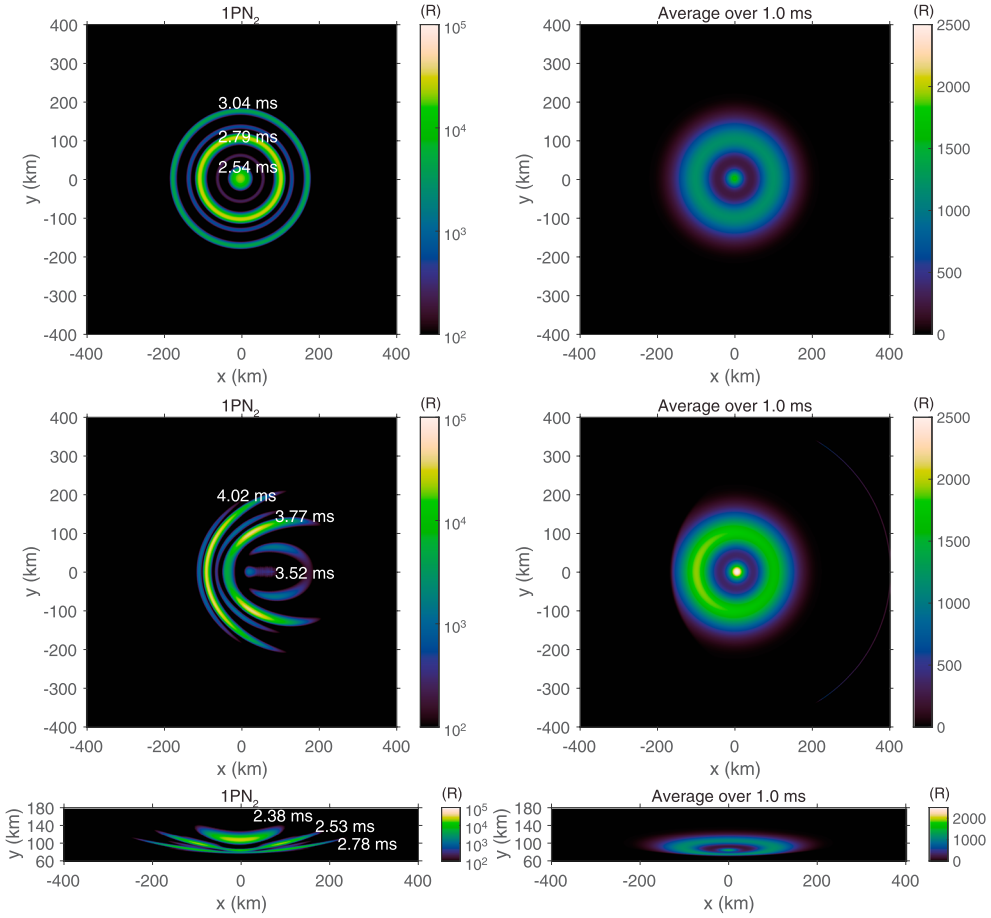

Figure 6. The elve, induced by an EIP pulse of 100 μs duration, projected at 90 km altitude when viewed from a spacecraft at 700 km altitude (top row) right above the center and (middle row) with a horizontal displacement of 700 km from the center. (bottom row) The elve projected on the *yz* plane, viewed from a point at $x = 600$ km. Taking into account Earth's curvature, the viewing point is at 28 km altitude. The left panels show the instantaneous emission intensity in rayleighs at selected moments of time, and the right panels show the intensity averaged over 1 ms.

difference is that there is also a bright emission region at the center, which is driven by the induction component of the electric field. Because this component is proportional to the current moment and both current moment waveforms have the same peak, a similar emission region should also exist for the shorter pulse case. However, the emission intensity of the concentric shells driven by the radiation component is much weaker for the longer pulse case, which makes the central emission region visible on the dynamic range of the intensity displayed in Figure 6.

It should be mentioned that Marshall (2012) found that high-peak current CGs with similar long, symmetric current waveforms can also produce elve doublets, but as pointed out by Marshall et al. (2015), such a current moment waveform is unrealistic for CGs because of the long rise time (Rakov & Uman, 2003, p. 7).

4. Discussion

4.1. Other Optical Emissions

As shown by Figure 1, the electric field can exceed $3E_k$ at elve altitudes. The $N_2(C)$ and $N_2^+(B)$ excited states emitting blue emissions of $2PN_2$ and $1NN_2^+$ band systems, respectively, are also produced at such a strong field. Their lifetimes are about 50 ns and 70 ns, much shorter than the width of the EMP pulse. As shown by Figure 7, the distributions of $N_2(C)$ and $N_2^+(B)$ densities show four distinct concentric shells, clearly separated from each other compared to the density distribution of $N_2(B)$ states shown in Figure 4. The shape of each concentric shell matches the corresponding wavefront of the EMP. However, when integrating along the line of sight to calculate the emission intensity, which typically does not overlap exactly with the wavefront, the two closely

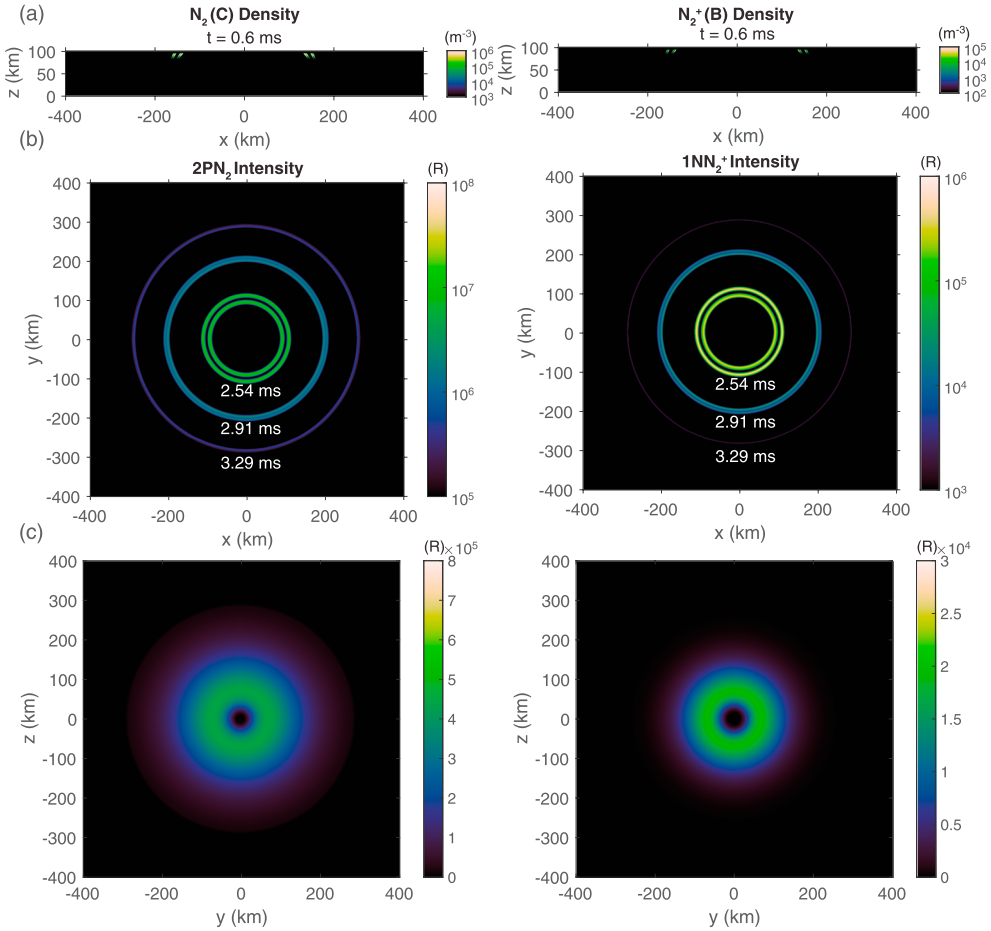

Figure 7. $2PN_2$ and $1NN_2^+$ emissions produced by the EIP of 11.2 μs duration. (a) The density distributions of $N_2(C)$ and $N_2^+(B)$ excited states. The instantaneous and average intensities of (b) $2PN_2$ and (c) $1NN_2^+$, when viewed from a spacecraft at 700 km altitude right above the center.

spaced concentric shells merge to form a single shell in the emission intensity distribution. Otherwise, the optical intensity distribution would have four bright concentric shells at every instant of time, forming an "elve quadruplet." The instantaneous and average intensities of $2PN_2$ reach ~10 MR and ~0.5 MR, while those of $1NN_2^+$ are ~500 kR and ~20 kR. The intensity of $2PN_2$ is comparable to the intensity of $1PN_2$, about a factor of 2 smaller, while the intensity of $1NN_2^+$ is about a factor of 50 smaller.

4.2. Effects of the Ionosphere Density Profile and Earth's Magnetic Field

The ambient ionospheric density profile considered in this study is based on the profile introduced by Wait and Spies (1964), and the parameters of h' and β have the average values inferred from remote sensing measurements (Hu et al., 2007). The values of h' and β of the nighttime lower ionosphere can vary significantly. A thin ionosphere allows the EMP to penetrate to higher ionospheric altitudes, and the resulting elve will be brighter because the normalized electric field E/E_k is larger and the coefficients of electron impact excitation are sensitive functions of E/E_k. Cummer et al. (2014) found that h' was 92 km for the TGF event associated with the shorter current pulse case. With this value, the resulting elve will be much brighter and occur at higher altitudes.

Earth's magnetic field is neglected in our study. According to Marshall (2012), the response of the lower ionosphere to the lightning EMP is mainly determined by the interaction of electrons and neutrals, and Earth's magnetic field plays a secondary role. The presence of Earth's magnetic field constrains electron motion and introduce anisotropy in the conductivity. When the electron neutral collision frequency is much higher than the electron gyrofrequency, or $\mu_e^2 B^2$ is much less than one where B is Earth's magnetic field, the effects of the magnetic field are negligible. With $0.3E_k$ electric field and 0.5 G magnetic field, $\mu_e^2 B^2 = 0.15$ at 85 km

altitude and $\mu_e^2 B^2 \simeq 1$ at 90 km altitude, so that it is reasonable to neglect the effects of Earth's magnetic field. In addition, μ_e is smaller at electric field greater than $0.3E_k$, which is required to generate a sufficiently bright elve. It should however be noted that including the effects of Earth's magnetic field in the simulation leads to asymmetric elves (Marshall et al., 2010).

4.3. TGF Durations and Elves

The durations of typical TGFs vary from tens to hundreds of microseconds (Briggs et al., 2010; Fishman et al., 2011; Foley et al., 2014). The analysis of the pulse shape by Foley et al. (2014) indicates that about 70% of TGFs have an asymmetric pulse shape, with the rise time shorter than the fall time. After taking into account the Compton scattering effects that are more significant for the photons arriving later, the authors concluded that the photon pulse at the source should be relatively symmetric, consistent with the modeling results of relativistic feedback discharges (Dwyer, 2012; Liu & Dwyer, 2013). The median rise time for the asymmetrical pulse is shorter and has a value of 43 μs.

The modeling results of relativistic feedback discharges show that the peak photon emission rate can be a few times larger for shorter TGFs than longer ones (Dwyer, 2012; Liu & Dwyer, 2013). On the other hand, the total fluences of TGFs of different durations are on the same order of magnitude (Dwyer et al., 2017). TGFs with shorter durations are expected to produce larger peak current moments, because the TGF discharge current is spread out over a shorter time (Dwyer, 2012; Dwyer & Cummer, 2013). Therefore, the peak of the current moment derivative for shorter TGFs is likely larger than that for longer TGFs. Therefore, elves are more likely to accompany TGFs with short durations.

4.4. EIP Elve Doublets Versus CID Elve Doublets

The cloud discharges causing NBEs (Marshall et al., 2015) or EIPs (this study) can produce elve doublets, because the discharges occur at cloud altitudes and the time separation between the direct and ground-reflected waves is sufficient to make distinct luminous shells. The differences in the properties of the source currents of those two types of IC discharges determine how the resulting elve doublets differ. The analysis of 44 days of IC events with an NLDN peak current greater than 200 kA found that there were about equal numbers of EIPs and negative-polarity NBEs (Lyu et al., 2015). The authors also concluded that the EIPs are different from the NBEs in several aspects. The properties that may make them produce different elves are the source height and duration. The average source altitude of the EIPs is about 6.4 km lower than that of the NBEs, with the NBEs likely originating between the upper positive and negative screening charge layers and the EIPs between the main negative and upper positive charge layers. This means that the reflected wave off the ground for the NBE can have an extra delay of up to 43 μs from the direct wave. Therefore, the two elves of the doublet produced by the EIP is less separated in space, and in time, than those produced by the CID, as viewed from any observing platform. It should be pointed out that the NBEs in the data set of the high-peak current events analyzed by Lyu et al. (2015) happen to be of negative polarity. CIDs that produce positive polarity NBEs can also generate high-peak currents. They typically occur between the two main thundercloud charge layers for normally electrified thunderstorms, and their altitudes are therefore similar to those of EIPs. The source altitude, which contributes to determining the separation in either space or time between the two elves of an elve doublet, alone is then insufficient to determine if it is caused by EIPs or CIDs. As discussed in the next section, the difference in the duration of their source discharges can give clues on whether an elve doublet is caused by an EIP or CID.

Marshall et al. (2015) also reported that the brightness of the first elve of an elve doublet is larger than that of the second elve for some cases, but smaller for other cases. According to the same study, it is generally difficult for a vertical CID discharge to produce a brighter second elve, and a solution to this problem is that if the CID discharge is oriented with an angle of 5° – 20° from the vertical, the second elve can be brighter.

The simulation for the shorter EIP pulse case indicates that the direct wave has a larger magnitude out to about 170 km horizontal range. Given that the average intensity distribution of the optical emissions is peaked at r <100 km, it means that the first elve has a larger brightness. The simulation of the longer pulse case shows that the second elve can have a larger brightness. Therefore, an alternative explanation to the relative brightness of the two elves of an elve doublet is that the source current pulse width varies in a wide range, such as that of EIPs. Since the peak current moment for the longer pulse case presented in section 3 is likely unrealistic, we have therefore conducted another simulation with a more realistic current moment waveform, which shows that the EIP elves can have unique features and is discussed in the next section.

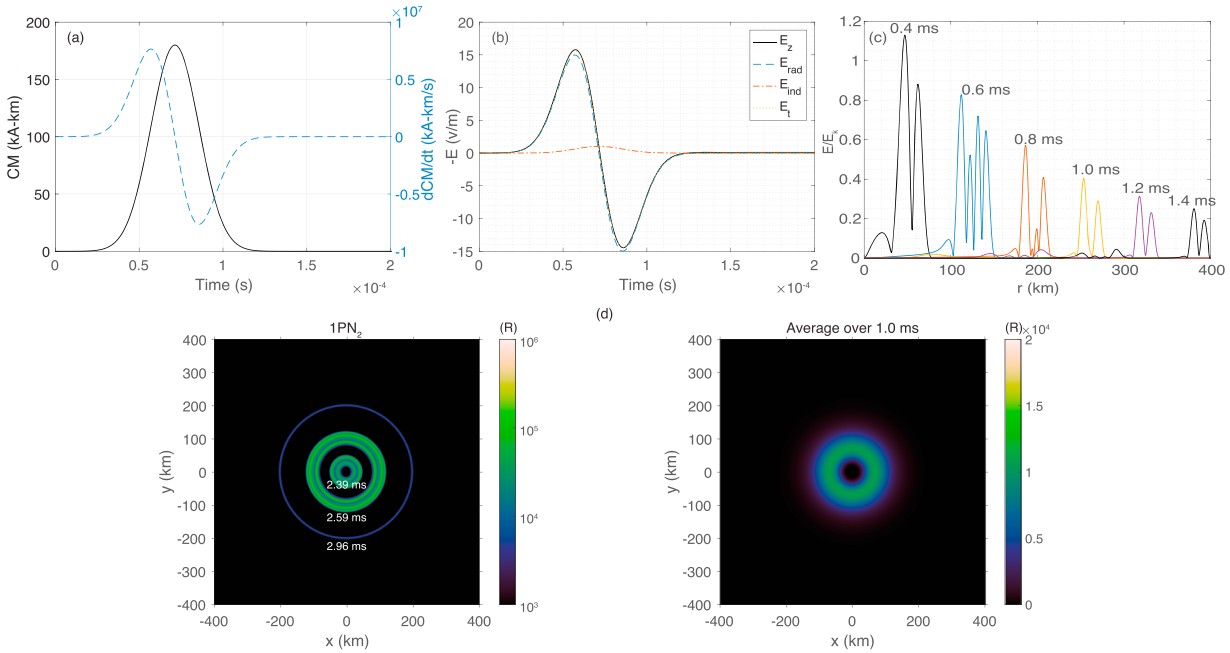

Figure 8. The source current waveform, electric field, and $1PN_2$ intensity distribution for an EIP pulse with 33.6 μs duration and 180 kA km peak current moment. (a) The current moment waveform and its time derivative. (b) The electric field on ground at a distance of 100 km. The solid line shows the field from simulation, the dashed and dash-dotted lines are analytical solutions of the radiation and induction components (Uman et al., 1975), and the dotted line is the sum of those two components. (c) The time evolution of the electric field profile at 94.5 km altitude, at which the normalized electric field, E/E_k, at $r = 100$ km has its maximum value over the entire simulation. (d) The instantaneous and average intensities of $1PN_2$, when viewed from a spacecraft at 700 km altitude right above the center.

4.5. Elve Quadruplets

The pulse duration of EIPs varies from ~10 to 100 μs, with an average pulse width of 55.1 μs, much longer than the 9.2 μs of the NBEs (Lyu et al., 2015), which is consistent with the durations of TGFs. In addition, the source current for the EIP pulses are relatively symmetric (Cummer et al., 2014), also consistent with the TGF photon waveforms, particularly for short TGFs, while typical NBEs have a fast rise and a slower decay. However, because the leading and trailing edges of the EMP of the shorter pulse case studied in the previous sections do not produce distinct signatures in the optical emissions, the difference in the shape of the waveform is not reflected in the appearance of the elve doublet. To further study the effects of the duration of the discharges responsible for TGF production or EIPs on the appearance of the elves, a simulation with an intermediate duration is performed.

For this simulation, the FWHM pulse width is increased by a factor of three from the shorter pulse case, while the peak current moment is reduced by the same factor. So the total charge moment change is the same. The results are shown in Figure 8. The field at $r = 100$ km on ground is about a factor of 9 smaller, consistent with the changes made to the current moment waveform. In order to have a sufficiently bright elve, a thinner ionosphere with $h' = 90$ km is used. The EMP penetrates deeper into the lower ionosphere, and the vertical profile of the normalized electric field, E/E_k, at $r = 100$ km has its maximum value at 94.5 km altitude. Figure 8c shows that there are two peaks initially, for example, at 0.4 ms, and also later when $t \geq 0.8$ ms. The lagging peak has a larger magnitude than the leading peak. Interestingly, at $t = 0.6$ ms, there are four peaks that are relatively well separated. The instantaneous intensity distributions of $1PN_2$ in Figure 8d are consistent with the radial profiles of the field. There are two rings at 2.39 ms, and four rings at 2.59 ms. At 2.96 ms, there is only one ring, because the smaller peak of the electric field is insufficient to excite N_2 molecules. It should also be noted that the first ring is not the brightest one. This simulation shows that the relative brightness of the elves of a doublet can also be explained by the variability in the duration of the source current and the ionosphere height.

The simulation also shows that elve quadruplets can be triggered by EIPs. The four elves of the elve quadruplet are most discernible from each other, when the four electric field peaks in Figure 8c are evenly spaced. The time separation between the direct and reflected waves decreases from ~80 to ~50 μs when the radial distance

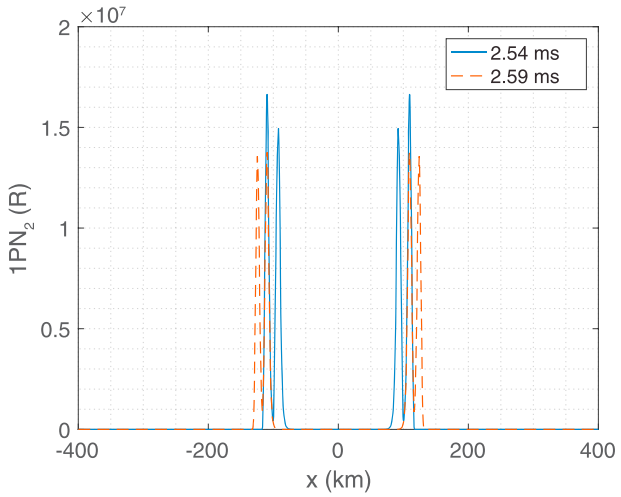

Figure 9. The profile of the $1PN_2$ intensity along the radial direction for the elve doublet shown in Figure 3.

increases from 0 to 100 km. Therefore, when the two extrema of the derivative of the current moment are separated by half of that time or ~25–40 μs, the four electric field peaks are approximately evenly spaced. This means that σ of the source Gaussian current moment waveform should be in the range of ~12.5–20 μs or the FWHM in the range of 30–47 μs. It should be pointed out that under a different viewing geometry, the multiplet feature may not be as clear as shown by Figure 8 because of the integration effects along the line of sight. For example, when viewed upward from a point at $x = 400$ km, only three distinct elves are visible (see Movies S4 and S5 included as supporting information).

Finally, since a significant fraction of TGFs have multiple pulses (e.g., Fishman et al., 1994; Fishman et al., 2011; Foley et al., 2014), it might be possible that multiple elve multiplets accompany a multi-pulsed TGF event.

4.6. Detection of EIP Elves

At 2.54 ms, the inner shell of the elve doublet shown in Figure 3 has a peak intensity of 15 MR at a radial distance of 92 km, while the outer shell has a peak intensity of 17 MR at 109.5 km. When viewed from an altitude of 700 km right above the elve, the angular separation between the two shells is about 1.6°; when viewed from the ground below, the separation is 5°. Figure 9 shows that the $1PN_2$ intensity profiles at 2.54 ms and 2.59 ms, indicating that a temporal resolution of at least 50 μs is required to differentiate the two elves. This value is consistent with the spatial separation between the two elves, (109.5 km−92 km)/$(3.0 \times 10^5$ km/s) = 58 μs.

The four elves of the elve quadruplet shown in Figure 8 at 2.59 ms have peak intensities of 93 kR at 91.5 km, 24 kR at 101.75 km, 107 kR at 110.5 km, and 50.75 kR at 118.5 km, respectively. The smallest spatial separation of two adjacent shells corresponds to an angular separation of 0.7° for spacecraft at 700 km altitude and 1.9° for the ground below. A temporal resolution of about 25 μs is required to differentiate two subsequent elve components.

Past ground- or satellite-based optical instruments were able to detect elve emissions of tens of kR (e.g., Barrington-Leigh et al., 2001; Kuo et al., 2007), so the EIP doublet or quadruplet should be bright enough to be detected. The required temporal resolution would be challenging to those instruments, with the fastest instruments having a resolution of 30–40 μs (Barrington-Leigh et al., 2001; Newsome & Inan, 2010). In addition, if viewed from a slanted direction, a better temporal resolution is needed to resolve the elve components.

Detection of the EIP elves can provide valuable information. First, reliable detection of EIPs requires low-frequency (LF) measurements, which have a limited range. Optical observations, particularly, from space can cover regions where nearby LF sensors are not available. Second, according to Lyu et al. (2016), there is a direct relationship between a subset of TGFs and EIPs. Therefore, optical elve observation may provide an alternative method to detect TGFs.

5. Summary and Conclusions

The simulations of the ionospheric responses to a class of high peak current IC flashes known as EIPs indicate that bright elves can be induced by the EMPs radiated by EIPs. Since there is growing evidence from recent work suggesting that TGFs are caused by EIPs, it means that TGFs, particularly those with short durations, can be accompanied by optical signatures in the lower ionosphere. In particular, our study has shown that the 25 September 2013 TGF detected by Fermi would have generated a bright elve. The findings of this study can be summarized as follows:

1. The optical intensity of the elves associated with EIPs can reach tens of millions of rayleighs. The red emissions from $1PN_2$ dominate, but significant blue emissions from $2PN_2$ and $1NN_2^+$ are also excited, with the corresponding intensity reaching ~10 MR and ~0.5 MR. Those intensity numbers are obtained from simulating an elve caused by one of the most intense EIPs reported under average nighttime ionosphere condition. Although a thinner ionosphere will allow the EMP of the EIP to penetrate deeper into the lower ionosphere,

increasing the peak of the normalized electric field in the lower ionosphere and more effectively producing excited states, those numbers are likely to be the upper limits of the intensities of the elves associated with TGFs.

2. The elves caused by EIPs with durations of ~10 μs are elve doublets. The first elve of the doublet is induced by the direct wave from the EIP, and the second elve by the ground-reflected wave. The first elve is typically brighter than the second elve. As the two elves expand radially, they will merge and form a single elve. For EIPs of longer durations, elve multiplets greater than two can be produced. An elve quadruplet is obtained with an EIP with a duration of 33.6 μs, and the four elves correspond to the rise and fall of the source current waveform and their reflections.
3. Bright and short TGFs are more likely to have accompanying elves, because their source current moment waveforms vary more rapidly and radiate stronger EMPs.

Acknowledgments
This research was supported in part by NSF grant AGS-1552177, NSF grant AGS-1348046, and AFOSR grant FA9550-16-1-0396 to the University of New Hampshire, and by NSF grant AGS-1565606 to Duke University. Disclaimer: The views expressed are not endorsed by the sponsors. The simulations used for this publication are available upon request from the authors (Ningyu.Liu@unh.edu). Videos showing the developments of the elve doublet presented in Figure 3 and the elve quadruplet in Figure 8 are available as supporting information.

References

Barrington-Leigh, C. P., Inan, U. S., & Stanley, M. (2001). Identification of sprites and elves with intensified video and broadband array photometry. *Journal of Geophysical Research*, *106*(A2), 1741–1750. https://doi.org/10.1029/2000JA000073

Blaes, P. R., Marshall, R. A., & Inan, U. S. (2016). Global occurrence rate of elves and ionospheric heating due to cloud-to-ground lightning. *Journal of Geophysical Research: Space Physics*, *121*, 699–712. https://doi.org/10.1002/2015JA021916

Blanc, E., Lefeuvre, F., Roussel-Dupré, R., & Sauvaud, J. A. (2007). TARANIS: A microsatellite project dedicated to the study of impulsive transfers of energy between the Earth atmosphere, the ionosphere, and the magnetosphere. *Advances in Space Research*, *40*, 1268–1275. https://doi.org/10.1016/j.asr.2007.06.037

Boeck, W. L., Vaughan, O. H., Blakeslee, R. J., Vonnegut, B., & Brook, M. (1992). Lightning induced brightening in the airglow layer. *Geophysical Research Letters*, *19*, 99–102.

Briggs, M. S., Fishman, G. J., Connaughton, V., Bhat, P. N., Paciesas, W. S., Preece, R. D., … Chekhtman, A. (2010). First results on terrestrial gamma ray flashes from the Fermi Gamma-ray Burst Monitor. *Journal of Geophysical Research*, *115*(A14), A07323. https://doi.org/10.1029/2009JA015242

Celestin, S., Xu, W., & Pasko, V. P. (2012). Terrestrial gamma ray flashes with energies up to 100 MeV produced by nonequilibrium acceleration of electrons in lightning. *Journal of Geophysical Research*, *117*(A16), A05315. https://doi.org/10.1029/2012JA017535

Cummer, S. A., Briggs, M. S., Dwyer, J. R., Xiong, S., Connaughton, V., Fishman, G. J., … Solanki, R. (2014). The source altitude, electric current, and intrinsic brightness of terrestrial gamma ray flashes. *Geophysical Research Letters*, *41*, 8586–8593. https://doi.org/10.1002/2014GL062196

Dwyer, J. R. (2003). A fundamental limit on electric fields in air. *Geophysical Research Letters*, *30*(20), 2055. https://doi.org/10.1029/2003GL017781

Dwyer, J. R. (2012). The relativistic feedback discharge model of terrestrial gamma ray flashes. *Journal of Geophysical Research*, *117*, A02308. https://doi.org/10.1029/2011JA017160

Dwyer, J. R., & Cummer, S. A. (2013). Radio emissions from terrestrial gamma-ray flashes. *Journal of Geophysical Research: Space Physics*, *118*, 3769–3790. https://doi.org/10.1002/jgra.50188

Dwyer, J. R., Liu, N. Y., Grove, J. E., Rassoul, H. K., & Smith, D. M. (2017). Characterizing the source properties of terrestrial gamma ray flashes. *Journal of Geophysical Research: Space Physics*, *122*, 8915–8932.

Dwyer, J. R., Liu, N., & Rassoul, H. K. (2013). Properties of the thundercloud discharges responsible for terrestrial gamma-ray flashes. *Geophysical Research Letters*, *40*, 4067–4073. https://doi.org/10.1002/grl.50742

Dwyer, J. R., Smith, D. M., & Cummer, S. A. (2012). High-energy atmospheric physics: Terrestrial gamma-ray flashes and related phenomena. *Space Science Reviews*, *173*, 133–196. https://doi.org/10.1007/s11214-012-9894-0

Fishman, G. J., Bhat, P. N., Mallozzi, R., Horack, J. M., Koshut, T., Kouveliotou, C., … Christian, H. J. (1994). Discovery of intense gamma-ray flashes of atmospheric origin. *Science*, *264*(5163), 1313–1316.

Fishman, G. J., Briggs, M. S., Connaughton, V., Bhat, P. N., Paciesas, W. S., von Kienlin, A., … Greiner, J. (2011). Temporal properties of the terrestrial gamma-ray flashes from the Gamma-Ray Burst Monitor on the Fermi Observatory. *Journal of Geophysical Research*, *116*(A15), A07304. https://doi.org/10.1029/2010JA016084

Foley, S., Fitzpatrick, G., Briggs, M. S., Connaughton, V., Tierney, D., McBreen, S., … Wilson-Hodge, C. (2014). Pulse properties of terrestrial gamma-ray flashes detected by the fermi gamma-ray burst monitor. *Journal of Geophysical Research: Space Physics*, *119*, 5931–5942. https://doi.org/10.1002/2014JA019805

Fukunishi, H., Takahashi, Y., Kubota, M., Sakanoi, K., Inan, U. S., & Lyons, W. A. (1996). Elves: Lightning-induced transient luminous events in the lower ionosphere. *Geophysical Research Letters*, *23*(16), 2157–2160.

Hu, W. Y., Cummer, S. A., & Lyons, W. A. (2007). Testing sprite initiation theory using lightning measurements and modeled electromagnetic fields. *Journal of Geophysical Research*, *112*, D13115. https://doi.org/10.1029/2006JD007939

Inan, U. S., Bell, T. F., & Rodriguez, J. V. (1991). Heating and ionization of the lower ionosphere by lightning. *Geophysical Research Letters*, *18*, 705–708. https://doi.org/10.1029/91GL00364

Inan, U. S., Cummer, S. A., & Marshall, R. A. (2010). A survey of ELF and VLF research on lightning-ionosphere interactions and causative discharges. *Journal of Geophysical Research*, *115*, A00E36. https://doi.org/10.1029/2009JA014775

Inan, U., & Inan, A. (2000). *Electromagnetic waves*. Upper Saddle River, NJ: Prentice Hall.

Inan, U. S., Sampson, W. A., & Taranenko, Y. N. (1996). Space-time structure of optical flashes and ionization changes produced by lighting-emp. *Geophysical Research Letters*, *23*(2), 133–136.

Kuo, C. L., Chen, A. B., Lee, Y. J., Tsai, L. Y., Chou, R. K., Hsu, R. R., … Fukunishi, H. (2007). Modeling elves observed by FORMOSAT-2 satellite. *Journal of Geophysical Research*, *112*, A11312. https://doi.org/10.1029/2007JA012407

Liu, N. Y., & Dwyer, J. R. (2013). Modeling terrestrial gamma ray flashes produced by relativistic feedback discharges. *Journal of Geophysical Research: Space Physics*, *118*, 2359–2376. https://doi.org/10.1002/jgra.50232

Liu, N. Y., McHarg, M. G., & Stenbaek-Nielsen, H. C. (2015). High-altitude electrical discharges associated with thunderstorms and lightning. *Journal of Atmospheric and Solar-Terrestrial Physics*, *136*, 98–118. https://doi.org/10.1016/j.jastp.2015.05.013

Liu, N. Y., & Pasko, V. P. (2004). Effects of photoionization on propagation and branching of positive and negative streamers in sprites. *Journal of Geophysical Research*, *109*, A04301. https://doi.org/10.1029/2003JA010064

Lu, G., Cummer, S. A., Li, J., Han, F., Smith, D. M., & Grefenstette, B. W. (2011). Characteristics of broadband lightning emissions associated with terrestrial gamma ray flashes. *Journal of Geophysical Research*, *116*(A15), A03316. https://doi.org/10.1029/2010JA016141

Lyu, F., Cummer, S. A., Briggs, M., Marisaldi, M., Blakeslee, R. J., Bruning, E., … Stanbro, M. (2016). Ground detection of terrestrial gamma ray flashes from distant radio signals. *Geophysical Research Letters*, *43*, 8728–8734. https://doi.org/10.1002/2016GL070154

Lyu, F., Cummer, S. A., & McTague, L. (2015). Insights into high peak current in-cloud lightning events during thunderstorms. *Geophysical Research Letters*, *42*, 6836–6843. https://doi.org/10.1002/2015GL065047

Marisaldi, M., Fuschino, F., Labanti, C., Galli, M., Longo, F., Del Monte, E., … Salotti, L. (2010). Detection of terrestrial gamma ray flashes up to 40 MeV by the AGILE satellite. *Journal of Geophysical Research*, *115*, A00E13. https://doi.org/10.1029/2009JA014502

Marshall, R. A. (2012). An improved model of the lightning electromagnetic field interaction with the D-region ionosphere. *Journal of Geophysical Research*, *117*, A03316. https://doi.org/10.1029/2011JA017408

Marshall, R. A., Inan, U. S., & Glukhov, V. S. (2010). Elves and associated electron density changes due to cloud-to-ground and in-cloud lightning discharges. *Journal of Geophysical Research*, *115*, A00E17. https://doi.org/10.1029/2009JA014469

Marshall, R. A., Silva, C. L., & Pasko, V. P. (2015). Elve doublets and compact intracloud discharges. *Geophysical Research Letters*, *42*, 6112–6119. https://doi.org/10.1002/2015GL064862

Moss, G. D., Pasko, V. P., Liu, N., & Veronis, G. (2006). Monte Carlo model for analysis of thermal runaway electrons in streamer tips in transient luminous events and streamer zones of lightning leaders. *Journal of Geophysical Research*, *111*, A02307. https://doi.org/10.1029/2005JA011350

Neubert, T., Kuvvetli, I., Budtz-Jørgensen, C., Østgaard, N., Reglero, V., & Arnold, N. (2006). The atmosphere-space interactions monitor (ASIM) for the international space station. In *ILWS (International Living With a Star) Workshop* (pp. 19–20). Goa, India.

Newsome, R. T., & Inan, U. S. (2010). Free-running ground-based photometric array imaging of transient luminous events. *Journal of Geophysical Research*, *115*, A00E41. https://doi.org/10.1029/2009JA014834

Oskooi, A. F., Roundy, D., Ibanescu, M., Bermel, P., Joannopoulos, J. D., & Johnson, S. G. (2010). MEEP: A flexible free-software package for electromagnetic simulations by the FDTD method. *Computer Physics Communications*, *181*, 687–702. https://doi.org/10.1016/j.cpc.2009.11.008

Pasko, V. P. (2010). Recent advances in theory of transient luminous events. *Journal of Geophysical Research*, *115*, A00E35. https://doi.org/10.1029/2009JA014860

Rakov, V. A., & Uman, M. A. (2003). *Lightning: Physics and Effects*. Cambridge, UK: Cambridge University Press.

Salem, M. A., Liu, N., & Rassoul, H. K. (2016). Modification of the lower ionospheric conductivity by thunderstorm electrostatic fields. *Geophysical Research Letters*, *43*, 5–12. https://doi.org/10.1002/2015GL066933

Smith, D. M., Lopez, L. I., Lin, R. P., & Barrington-Leigh, C. P. (2005). Terrestrial gamma-ray flashes observed up to 20 MeV. *Science*, *307*(5712), 1085–1088. https://doi.org/10.1126/science.1107466

Uman, M. A., McLain, D. K., & Krider, E. P. (1975). The electromagnetic radiation from a finite antenna. *American Journal of Physics*, *43*, 33–38. https://doi.org/10.1119/1.10027

Veronis, G., Pasko, V. P., & Inan, U. S. (1999). Characteristics of mesospheric optical emissions produced by lightning discharges. *Journal of Geophysical Research*, *104*(A6), 12,645–12,656.

Wait, J. R., & Spies, K. P. (1964). Characteristics of the Earth-ionosphere waveguide for VLF radio waves (*Tech. Note 300*). Boulder, Colo.: National Bureau of Standards. Dec. 30.

Xu, W., Celestin, S., & Pasko, V. P. (2015). Optical emissions associated with terrestrial gamma ray flashes. *Journal of Geophysical Research: Space Physics*, *120*, 1355–1370. https://doi.org/10.1002/2014JA020425

Xu, W., Celestin, S., Pasko, V. P., & Marshall, R. A. (2017). A novel type of transient luminous event produced by terrestrial gamma-ray flashes. *Geophysical Research Letters*, *44*, 2571–2578. https://doi.org/10.1002/2016GL072400